Atmospheric
Measurement
Techniques
Open Access
Discussions

Coupling sky images with three-dimensional radiative transfer models: a new method to estimate cloud optical depth

F. A. Mejia, B. Kurtz, K. Murray, L. M. Hinkelman, M. Sengupta, Y. Xie, and J. Kleissl

Center for Renewable Resources and Integration, Department of Mechanical and Aerospace Engineering, University of California, San Diego 9500 Gilman Dr., La Jolla, CA 92093, USA

Correspondence to: J. Kleissl (jkleissl@ucsd.edu)

Title Page

Abstract	Introduction
Conclusions	References
Tables	Figures

|◄ | ►|
◄ | ►
Back | Close

Full Screen / Esc

Printer-friendly Version

Interactive Discussion

Title Page

Abstract | Introduction

Conclusions | References

Tables | Figures

|◄ | ►|

◄ | ►

Back | Close

Full Screen / Esc

Printer-friendly Version

Interactive Discussion

Abstract

A method for retrieving cloud optical depth (τ_c) using a ground-based sky imager (USI) is presented. The Radiance Red-Blue Ratio (RRBR) method is motivated from the analysis of simulated images of various τ_c produced by a 3-D Radiative Transfer Model (3DRTM). From these images the basic parameters affecting the radiance and RBR of a pixel are identified as the solar zenith angle (θ_0), τ_c, solar pixel angle/scattering angle (ϑ_s), and pixel zenith angle/view angle (ϑ_z). The effects of these parameters are described and the functions for radiance, $I_\lambda(\tau_c, \theta_0, \vartheta_s, \vartheta_z)$ and the red-blue ratio, RBR($\tau_c, \theta_0, \vartheta_s, \vartheta_z$) are retrieved from the 3DRTM results. RBR, which is commonly used for cloud detection in sky images, provides non-unique solutions for τ_c, where RBR increases with τ_c up to about $\tau_c = 1$ (depending on other parameters) and then decreases. Therefore, the RRBR algorithm uses the measured $I_\lambda^{\text{meas}}(\vartheta_s, \vartheta_z)$, in addition to RBR$^{\text{meas}}(\vartheta_s, \vartheta_z)$ to obtain a unique solution for τ_c. The RRBR method is applied to images taken by a USI at the Oklahoma Atmospheric Radiation Measurement program (ARM) site over the course of 220 days and validated against measurements from a microwave radiometer (MWR); output from the Min method for overcast skies, and τ_c retrieved by Beer's law from direct normal irradiance (DNI) measurements. A τ_c RMSE of 5.6 between the Min method and the USI are observed. The MWR and USI have an RMSE of 2.3 which is well within the uncertainty of the MWR. An RMSE of 0.95 between the USI and DNI retrieved τ_c is observed. The procedure developed here provides a foundation to test and develop other cloud detection algorithms.

1   Introduction

Advances in solar photovoltaic (PV) technologies have paved the way for higher PV penetration but as we rely more heavily on solar energy it becomes ever more crucial to understand the characteristics of this energy source. Unlike fossil fuels, solar energy has an inherent variability that causes difficulty when integrating solar energy into the

F. A. Mejia et al.

grid. Improving forecasting of the available solar irradiance will support management of the electric grid and electricity markets and therefore ensure a more economical integration of solar power (Mathiesen et al., 2013). Currently several different methods are used to forecast at different spatial and temporal resolutions including numer-

5 ical weather prediction (e.g. Lorenz et al., 2009; Mathiesen et al., 2011), and satellite image-based forecasting (e.g. Hammer et al., 1999). For short term forecasting, whole-sky imagery has been used (e.g. Urquhart et al., 2013).

Physics-based solar forecasting using whole-sky imagery requires geolocating clouds in the sky images, estimating their optical depth, motion, and dynamics (Chow

10 et al., 2011). To estimate cloud optical depth (τ_c), the most advanced methods separate the image into clear sky, thin cloud and thick cloud and assign a τ_c to each of these groups. To distinguish thin and thick clouds, the red-blue ratio (RBR; or a function of RBR) has been used as the default method (Koehler et al., 1991; Shields et al., 1993; Chow et al., 2011; Ghonima et al., 2012; Roy et al., 2001). It is defined as the ratio of

15 the signal from the red channel to the signal from the blue channel. The RBR method takes advantage of Rayleigh scattering being greater in the blue wavelengths than the red wavelengths. When Rayleigh scattering is the predominant form of scattering, such as in clear skies, the RBR for a given view angle is smaller than under cloud scattering. RBR successfully differentiates clear sky from thin clouds and to a more limited extent

20 thick clouds, but the RBR has not been applied to differentiate τ_c. It is also difficult to apply the RBR method in the circumsolar region as thick dark clouds have lower RBRs than clear sky (Chow et al., 2011). In fact we will demonstrate in this paper through radiative transfer modeling (Sect. 4) that RBR by itself is ineffective for differentiating τ_c even for homogeneous cloud layers.

25 Most current cloud detection methods are designed empirically using look-up tables and/or thresholds that are adjusted to "work" with a specific imager and cloud conditions (see Sect. 2). The present paper breaks new ground in that it attempts to improve our fundamental understanding of the impact of three-dimensional radiative transfer (3D-RT) and τ_c on the radiance and RBR of a given pixel in a sky image. To analyze

this relation, the Spherical Harmonic Discrete Ordinate Method (SHDOM; Evans et al., 1998; Pincu. 3) and analyze the determinants of sky imager radiances (Sect. 4). The results reveal non-linearities and non-monotonic behavior in radiances and RBR that explain many of the challenges previously observed with empirical cloud detection methods. The insights gained through 3D-RT are utilized to develop a τ_c retrieval algorithm for sky imagery (Sect. 5). The algorithm is validated in Sect. 6 and a discussion and conclusions are presented in Sect. 7.

2 Review of sky imager cloud detection methods and geometrical factors

Individual pixel cloud detection using the output image from sky imagers is based on either the radiance measurement or the ratio between radiance measurements for different wavelengths. Cloud detection algorithms using single channel radiance have found limited success (McGuffe et al., 1989; Kegelmeyer et al., 1994) due to the similarities in radiance values between clear skies and thick clouds in the visible spectrum. More success has been obtained when cloud detection uses the ratio between radiance measurements at different wavelength bands. One such algorithm is the RBR method, which uses the ratio of camera measurement in the red channel to the blue channel to classify a pixel as cloudy or clear. Initially a fixed RBR threshold between clear sky and cloudy sky (Koehler et al., 1991) is used which led to successful identification of opaque clouds but consistently failed to distinguish between thin and clear skies. However, the ratio of observed RBR to the clear sky RBR is fairly constant between contrail cases and provided a good way to identify thin clouds (Koehler et al., 1991). This lead to the development of clear sky libraries (CSL; Shields et al., 1993; Chow et al., 2011) to express clear sky RBR value under any condition. CSL are constructed by binning pixel values from clear sky images into matrices as a function of solar zenith angle (θ_0, Fig. 1), solar pixel angle/Scattering angle (ϑ_s) and pixel zenith angle/view angle (ϑ_z). Figure 1 demonstrates a diagram of the camera optics as well as solar and sky geometry. From the CSL it is then possible to simulate a clear sky

(Fig. 2a) for any given day, allowing the calculation of the ratio of measured RBR to clear sky RBR. A clear sky image reconstructed from the CSL, as well as the ϑ_s and the ϑ_z for an example image are illustrated in Fig. 2.

Gauchet et al. (2012) used a different approach to account for the directional effects in cloud detection, in which they segmented images into five zones, solar disk, circumsolar disk, extended circumsolar disk, main zone, sky horizon, and orographic horizon, each with its own radiance and red-blue difference (RBD) threshold separating clear sky, bright cloud, and dark cloud.

The red-blue difference (RBD, Heinle et al., 2010) uses the same principles as the RBR for cloud detection but attempts to eliminate the strong directional variability in the RBR due to variability in the radiance, $I_{\Delta\lambda}$, of the blue channel as seen in Eqs. (1, 2),

$$\text{RBR} = \frac{I_r}{I_b} = 1 + \frac{I_r - I_b}{I_b}, \tag{1}$$

$$\text{RBD} = I_r - I_b = I_b(\text{RBR} - 1), \tag{2}$$

where I_r is the $I_{\Delta\lambda}$ in the red channel, and I_b is the $I_{\Delta\lambda}$ in the blue channel. However, Ghonima et al. (2012) found minimal differences in performance between RBD and RBR retrieval with RBR outperforming RBD.

These approaches have led to improved accuracy of cloud detection, yet limited progress has been made to attempt to understand the phenomena that influence the performance of these various methods. Although a direct relationship with aerosol optical depth (τ_a) and RBR is observed for small τ_a, ($\tau_a < 0.3$; Ghonima et al., 2012) no direct relationship has been found between RBR, or other variables determined from sky imagers, and larger optical depths (τ) such as those found typically in clouds which has limited sky imager cloud detection to a binary classification. The lack of research on τ_c classification also stems from the fact that τ_c are challenging to measure accurately and large spatio-temporal variability and 3-D effects of cloud scattering make it difficult to conduct controlled case studies. Instead, a 3-D radiative transfer model is

Title Page

Abstract | Introduction

Conclusions | References

Tables | Figures

|◄ | ►|

◄ | ►

Back | Close

Full Screen / Esc

Printer-friendly Version

Interactive Discussion

applied here to investigate the interrelationships between radiances, radiance ratios (RBR), and τ_c and devise a method to detect τ_c.

3 Radiative transfer modeling of sky images and comparison to measurements

3.1 SHDOM model and input parameters

Because of the 3-D dependency of the sky radiance field, a 3D-RT model must be used to simulate sky images. SHDOM is an explicit 3D-RT model that uses discrete ordinates to integrate the radiative transfer equation spatially, while spherical harmonics are used to save memory when solving the source function. This method allows for better computational efficiency compared to other methods such as the Monte Carlo (MC) method when solving the whole sky radiance field. SHDOM is also found to be within 2–3 % of the MC models as part of the Intercompparison of 3-D Radiation Codes (I3RC) which is close to the MC noise (Marshak et al., 2005; Cahalan et al., 2005). Because of its computational efficiency and accuracy, SHDOM is selected for this analysis. SHDOM radiative transfer calculations are performed for 161 overcast skies with homogeneous τ_c, ranging in τ_c from 0 to 80 at solar zenith angles ranging from 21 to 70° and for wavelengths corresponding to the peaks of the USI camera's red (620 nm), green (520 nm) and blue (450 nm) channels.

Yearly average Aerosol Robotic Network (AERONET) data from the ARM Southern Great Plains (SGP) site for the year of 2013 for aerosol effective radius, and refractive index is used to calculate the single scattering properties of the aerosols in the SHDOM simulation (Holben et al., 1998; Holben et al., 2001; Table 1). Background Rayleigh and aerosol optical depths are also obtained from yearly averages taken from the sun-tracking photometer at the ARM SGP site. A cloud droplet effective radius of 8 μm (Min et al., 2003), is used to obtain the single scattering properties of the clouds in the SHDOM simulations. Given the desired τ_c, LWC is computed as (Stephens et al.,

1978),

$$\text{LWC} \approx \frac{\frac{2}{3}\,\tau_c\,\rho_l r_e}{\Delta z}, \tag{3}$$

where ρ_l is the density of liquid water and $\Delta z = 1\,\text{km}$ is the cloud geometric thickness. Cloud liquid water content (LWC) is assumed constant between a cloud base of 1 km and cloud top of 2 km.

The SHDOM output radiance field is used to reproduce a sky image that would be obtained through a fisheye lens with an equisolid angle projection (Miyamoto et al., 1964),

$$r' = 2f \sin\left(\frac{\vartheta_z}{2}\right) \tag{4}$$

where f is the focal length, and r' is the distance from the principal point in the image plane. Since SHDOM outputs a radiance field the USI signal output in counts must be calibrated to radiance.

3.2 USI hardware and calibration of the signal to radiance

On 14 March 2013 we deployed two USIs (serial numbers 1.7 and 1.8) at the ARM SGP site. The instrument domes were cleaned weekly. Daytime images from the USIs were collected continuously every 30 s for 220 days. Since USI 1.8 was located closer (at 200 m distance) to the instruments used for validation, it is used for the analysis. The optical setup included a Sigma 4.5 mm fisheye lens, an IR filter, and an Allied Vision GE2040 CCD camera (Fig. 1). The fisheye lens creates an equisolid angle projection onto the CCD resulting in an image where the solid angle subtended on each CCD cell (pixel) is approximately constant. Custom apertures were inserted into the lens of both USIs with diameters of 700 and 1000 μm for USI 1.7 and 1.8, respectively. A Bayer color filter on the CCD separates pixels into red, green and blue pixels allowing for

multispectral images. Three different images are taken at different exposure times and combined to create a high dynamic range (HDR) image (Urquhart et al., 2015). The signal measured by each pixel is related to the amount of photons that are transmitted through the optics and converted to a voltage. The signal measured can therefore be

5 calibrated to estimate the irradiance, $E_{\Delta\lambda}$ at a wavelength band, incident on a pixel. The radiance $I_{\Delta\lambda}^{\text{meas}}$ observed by each pixel can then be calculated using

$$I_{\Delta\lambda}^{\text{meas}} = \frac{E_{\Delta\lambda}}{\Delta\Omega\Delta\lambda} = \frac{C_{1\lambda}\cdot v}{\Delta t\, A_{\text{in}}\, \Delta\Omega\, \Delta\lambda} = C_{2\lambda}\cdot v, \tag{5}$$

where v is the camera measurement in counts at a given pixel, $C_{1\lambda}$ (units of J/count) is a calibration factor between v and $E_{\Delta\lambda}$, $C_{2\lambda}$ (units of $\text{W}\,\text{m}^{-2}\,\text{st}^{-1}\,\text{nm}^{-1}$) is a calibration

10 factor between v and $I_{\Delta\lambda}^{\text{meas}}$, A_{in} is the area of the pixel, $\Delta\Omega$ is the solid angle, and $\Delta\lambda$ is the wavelength band. Given the equisolid angle lense, A_{in}, $\Delta\Omega$ and $\Delta\lambda$ are constant across the image sensor, resulting in a linear relationship (ignoring optical errors, and camera sensor nonlinearities) between the camera's signal v and the radiance $I_{\Delta\lambda}$ at the pixel's ϑ_z as

15 $$C_{2\lambda} = \frac{\overline{I_{\Delta\lambda}(\vartheta_z,\vartheta_s)}}{v(\vartheta_z,\vartheta_s)}, \tag{6}$$

The calibration constant $C_{2\lambda}$ is obtained as the average (denoted as overbar in Eq. 6) of 131 all overcast (cloud fraction (CF) is greater than 0.9) images on 98 different days. Overcast skies are preferred because the radiance is more homogeneous and since the more robust method by Min et al. (2003) could be applied to ob-

20 tain the τ_c that is input to SHDOM. $C_{2\lambda}$ values are 1.16×10^{-4} , 1.11×10^{-4}, and $9.69 \times 10^{-5}\,\text{W}\,\text{m}^{-2}\,\text{st}^{-1}\,\text{nm}^{-1}$ for the red, green and blue channels, respectively.

3.3 Application to other imaging systems

Other ground imaging designs have also been developed (Seiz et al., 2007; Souza-Echer et al., 2006; Calbo et al., 2008; Cazorla et al., 2008; Heinle et al., 2010; Roman et al., 2012; Gauchet et al., 2012) with the most dissimilar design consisting of a downward pointing camera capturing the sky from a reflection off a spherical mirror (Pfister et al., 2003; Kassianov et al., 2005; Long et al., 2006; Mantelli et al., 2010; Martinez-Chico et al., 2011). Most ground imaging devices follow a relationship between the camera's signal and radiance similar to Eq. (1) differing only in the wavelength region $\Delta\lambda$, calibration factors C_{1_λ}, and C_{2_λ} and optical and sensor errors, with non-equisolid lens camera systems requiring $\Delta\Omega$, to be specified per pixel. Therefore the method presented here can be adapted easily to images from other sky imaging systems.

3.4 Comparison of real and synthetic (SHDOM) images and stray light correction

Example measured images and their SHDOM equivalent images are illustrated in Fig. 3. Differences between the clear sky image (Fig. 3a) and the synthetic image (Fig. 3b) highlight the impacts of stray light as well as the vertical smear stripe caused by the CCD sensor (Fig. 3c). The error observed in the solar disk is caused by errors in the geometrical calibration causing the solar location to be slightly different between the SHDOM and the USI image. The stray light is particularly strong in the circumsolar region causing enhancement of the red radiance of up to 30 %. Stray light is caused by light from the direct beam being scattered through the optics (mainly the protective acrylic dome). This means that stray light is strongest for τ_c near 0 and should decrease to zero once clouds are thick enough to eliminate the direct beam. Particular optical reflections are observed as circular patterns throughout the image that are concentrated at the solar azimuth. While stray light patterns are often consistent for the same sun position, misalignments in the camera optics (e.g. during instrument maintenance) can lead to stray light changing under constant ϑ_s, and ϑ_z making it difficult to implement a

general stray light correction, for example through a look-up table. Stray light leads to brighter pixel values than are expected, which in turn can lead to misclassifications of clear sky as thin clouds ($\tau_c < 3$). To mitigate some of the stray light effects the SHDOM results for clear sky ($\tau_c = 0$) are replaced by the measurements from the CSL to obtain the interpolant described in Sect. 5.

Figure 3d–f demonstrates USI images and a synthetic image from SHDOM for τ_c of 30. The majority of the sky ($\vartheta_z < 80°$) red radiance differs by less than 5 %. At $\tau_c = 30$ direction normal irradiance is absent and stray light is not present.

4 Impact of geometrical parameters and cloud optical depth on radiance and RBR

As described in Sect. 2 individual channel radiance and RBR are the most fundamental parameters for cloud detection in sky images. To obtain τ_c, the functions $I_\lambda(\tau_c)$ and RBR(τ_c) must be parameterized. Furthermore, geometrical parameters (ϑ_z, ϑ_s), and solar position (θ_0) have been found to affect RBR(τ_c) and $I_\lambda(\tau_c)$ (Shields et al., 1993) such that we must obtain RBR($\tau_c, \theta_0, \vartheta_s, \vartheta_z$) and $I_\lambda(\tau_c, \theta_0, \vartheta_s, \vartheta_z$) to solve the inverse problem. With the aid of the SHDOM it is possible to analyze each of these parameters individually. In this section, we will discuss example cases under various ϑ_s, ϑ_z, and θ_0 to demonstrate how each variable affects I_λ and RBR.

4.1 Solar pixel angle

Figure 4a demonstrates for the red and blue channel that radiance decreases with increasing ϑ_s for non-thick clouds ($\tau_c < 30$). For thin clouds ($\tau_c = 1$) the radiance peaks in the solar region as a result of the forward scattering peak of the cloud phase function. As τ_c increases, radiance becomes constant with ϑ_s.

Figure 4a shows that the blue radiance is larger than the red radiance under clear skies, except for very small ϑ_s, while for cloudy skies the two radiances are more sim-

ilar. Therefore, most cloud detection methods assume that RBR is higher for clouds than for clear sky; however, Fig. 4b demonstrates that this is not always the case. At small ϑ_s ($\vartheta_s < 6°$) the RBR of thick clouds is lower than that of clear sky. Moreover, as demonstrated by the $\tau_c = 1$ case thin clouds have a higher RBR at $\vartheta_s < 30°$ than thick clouds. For $\tau_c < = 10$ RBR increases as ϑ_s approaches the solar region. At higher τ_c ($\tau_c > = 30$) RBR becomes constant over ϑ_s. Note that all of the statements in Sect. 4 strictly only apply for the θ_0 and ϑ_z shown in the figure, but Figs. 4–6 indicate that the conditions $\theta_0 = = 60°$, $\vartheta_s = 60°$, $\vartheta_z = 60°$ are representative for a wide range of conditions.

4.2 Sky imager zenith angle

Near the horizon (large ϑ_z), diffuse irradiance is commonly observed to be enhanced. Horizon brightening is indeed observed for clear skies in Fig. 5a. As clouds become thicker the dependence of radiance on ϑ_z is inverted and radiance decreases with increasing ϑ_z. The radiative transfer transitions into the diffusion regime, where it is only dependent on ϑ_z. On the other hand the RBR dependence has a similar shape independent of the τ_c (Fig. 5b). Pixels near zenith have lower RBR than those near the horizon.

4.3 Solar zenith angle

The effects of θ_0 are intuitive and consistent to what is observed during a sunset and therefore not graphically presented; the red and blue radiance is observed to decrease with increasing θ_0. The decrease in radiance is caused by the decrease in extraterrestrial horizontal flux as θ_0 increases. On the other hand, RBR is found to increase with increasing θ_0, reflecting the increase in airmass with increasing θ_0. Increased airmass causes more blue light to be scattered back into space than red light.

4.4 Cloud optical depth

Figure 6a illustrates the ambiguity that arises when attempting to differentiate cloud optical depth with radiance. Radiance reaches a peak at $\tau_c = 3.25$ and almost for the entire range of τ_c there are two τ_c that lead to the same radiance. Figure 6b on the other hand, demonstrates the ambiguity of τ_c detection using only RBR. SHDOM simulations demonstrate that as τ_c increases RBR increases until it reaches its maximum around $\tau_c = 2$ and then decreases until converging to a constant value for $\tau_c > 20$. This creates the following challenges: (i) RBR is insensitive to cloud τ_c for $\tau_c > 20$ and therefore thick clouds of different τ_c cannot be distinguished. (ii) There is ambiguity because of the non-monotonic behavior. For example, clouds with a τ_c of 1.5 have similar RBR values to clouds of $\tau_c > 20$. While (outside the solar region, see Fig. 4b) RBR is a useful differentiator between clouds and clear sky more information is needed to differentiate between different τ_c.

Note that while Fig. 6a and b demonstrate the radiance and RBR for a section of the sky these curves change throughout the sky. The dependence is illustrated for a few geometric cases through the τ_c for which the peak in the red radiance is observed. In the circumsolar region red radiance peaks at $\tau_c \sim 0.75$ while clear sky has a higher radiance than thick clouds ($\tau_c > 5$). A similar trend is observed for RBR, where clear sky has a higher RBR than thick clouds ($\tau_c > 5$). Approaching $\vartheta_z = 0°$ and on the opposite side of the sun ($\vartheta_s > 60°$), the red radiance peaks at $\tau_c = 8.75$. Near the horizon ($\vartheta_z > 80°$) the red radiance peaks again at lower $\tau_c = 1.25$.

In addition, Fig. 6a highlights one of the main challenges of ground based images compared to satellite based cloud detection. In satellite based τ_c detection, the measured radiance can be used to calculate τ_c (Nakajima et al., 1990) as the measured (upwelling) radiance monotonically increases with higher τ_c. This same method cannot be used for ground based imagery as radiance increases for thin clouds peaks and then begins to decrease. This means that there can exist two τ_c that produce the same radiance. It is again important to also note that the curves in Fig. 6 depend on ϑ_s and

ϑ_z. For example, near the horizon ($\vartheta_z > 80°$), the radiances are in fact highest for clear skies and decrease with increasing τ_c.

4.5 Expressing cloud optical depth through geometrical and solar parameters

Since it is currently computationally infeasible to use SHDOM to solve $\tau_c(I_\lambda, \text{RBR}, \theta_0, \vartheta_s, \vartheta_z)$ in real-time ($\sim 10\,\text{s}$) as required for sky imager solar forecasting, the homogeneous cases described in Sect. 1 are used instead to create interpolants. As seen in Fig. 6a and b. $\tau_c(I_\lambda, \theta_0, \vartheta_s, \vartheta_z)$ and $\tau_c(\text{RBR}, \theta_0, \vartheta_s, \vartheta_z)$ are multivalued functions. Therefore two separate interpolants are created for each function. $\tau_c(I_\lambda, \theta_0, \vartheta_s, \vartheta_z)$ is split into τ_c that are higher than the peak radiance and τ_c that are lower than the peak radiance. $\tau_c(\text{RBR}, \theta_0, \vartheta_s, \vartheta_z)$ is similarly split into τ_c that are higher than the peak RBR and τ_c that are lower than the peak RBR. Section 5 will describe how these interpolants are used to find up to two $\tau_c(I_\lambda^{\text{meas}})$ (one for the higher and one for the lower branch of τ_c) and how a unique τ_c is obtained.

5 Radiance red blue ratio (RRBR) method for cloud optical depth measurement

We have shown that it is difficult to distinguish between different τ_c by using RBR alone. As demonstrated in Fig. 6 radiance and RBR are non-monotonic functions of τ_c with generally two τ_c associated with the same radiance or RBR. However, for most cases, there is a unique τ_c solution for a pair of RBR and radiance. The RRBR method attempts to obtain this solution by first solving $\tau_c(I_\lambda, \theta_0, \vartheta_s, \vartheta_z)$ and then substituting the (usually two) τ_c solutions into $\text{RBR}(\tau_c, \theta_0, \vartheta_s, \vartheta_z)$ and identifying the correct τ_c as the one with the smallest $\text{abs}(\text{RBR}^{\text{meas}}(\vartheta_s, \vartheta_z) - \text{RBR}(\tau_c, \theta_0, \vartheta_s, \vartheta_z))$, where $\text{RBR}^{\text{meas}}(\vartheta_s, \vartheta_z)$ is the measured RBR. The algorithm for the RRBR method is described in Fig. 7. I_λ at a wavelength of 620 nm is used because its variations with τ_c are larger than the other wavelengths. This larger dynamic range reduced the errors caused by instrument noise.

The algorithm begins by comparing $I_{620}^{\mathrm{meas}}(\vartheta_s, \vartheta_z)$ against $\max(I_{620}(tau_c, \theta_0, \vartheta_s \vartheta_z))$ (e..g $0.19\,\mathrm{W\,m^{-2}\,sr^{-1}\,nm^{-1}}$ in Fig. 6a), where $I_{620}^{\mathrm{meas}}(\vartheta_s, \vartheta_z)$ is the measured radiance in the camera's red channel. Heterogeneity in clouds can cause $I_{620}^{\mathrm{meas}}(\vartheta_s, \vartheta_z)$ to be larger than $\max(I_{620}(\tau_c, \theta_0, \vartheta_s, \vartheta_z))$; in this case as the pixel conditions fall outside the range of the method the algorithm reverts back to τ_c assignment solely based on RBR. $\tau_c(\mathrm{RBR}, \theta_0, \vartheta_s, \vartheta_z)$ is used to find τ_c. If there are two solutions, then the τ_c associated with the maximum red radiance is used as there is no way to differentiate between the multiple solutions.

If $I_{620}^{\mathrm{meas}}(\vartheta_s, \vartheta_z)$ is within the range of $I_{620}(\tau_c, \theta_0, \vartheta_s, \vartheta_z)$, then τ_c is calculated from $\tau_c\left(I_{620}^{\mathrm{meas}}, \theta_0, \vartheta_s, \vartheta_z\right)$. If only one solution is found the τ_c is assigned based on $\tau_c\left(I_{620}^{\mathrm{meas}}, \theta_0, \vartheta_s, \vartheta_z\right)$ and $\mathrm{RBR}(\tau_c, \theta_0, \vartheta_s, \vartheta_z)$ is not considered. When two solutions are found, they are input into $\mathrm{RBR}(\tau_c, \theta_0, \vartheta_s, \vartheta_z)$ and the one closest to $\mathrm{RBR}^{\mathrm{meas}}(\vartheta_s, \vartheta_z)$ is assigned. Note that since saturated pixel values near the sun exceed the dynamic range of the USI sensor, the RBR defaults to 1, the red radiance is unknown, and no τ_c can be assigned.

An example τ_c estimate is presented in Fig. 8. The darker clouds are correctly identified as higher τ_c, even though the RBR is lower than for the thinner clouds, for example for the clouds between the sun and the horizon. In the circumsolar region, the RBR is largest but the RRBR method correctly identifies a thinner cloud. The black points in Fig. 8b corresponds to undetermined τ_c due to signal saturation. In practice one could interpolate across the saturated region, but we prefer showing the raw results in this paper.

Although the RRBR method is developed from overcast scenarios we also apply this method to broken clouds. Errors are caused by 3-D effects near cloud edges, but are minimal for areas of the clouds far from cloud edges, where clouds may be considered locally homogeneous. An additional source of error is the τ_a used in the reference SHDOM simulations; higher actual τ_a values than those in the simulations may lead to τ_a being classified as τ_c, while smaller τ_a lead to a reduced τ_c estimate. This error is minimal since τ_c is much larger than the variations in τ_a. Furthermore, this error is not

Title Page

Abstract | Introduction

Conclusions | References

Tables | Figures

|◄ | ►|

◄ | ►

Back | Close

Full Screen / Esc

Printer-friendly Version

Interactive Discussion

important for solar forecasting as – spectral effects aside – only the total atmospheric optical depth is of interest to estimate ground irradiance, not the exact differentiation between τ_a and τ_c.

6 Validation

6.1 Cloud optical depth measurements for validation

The Min method (Min et al., 1996b, 2003) is designed to estimate τ_c for conditions with homogenous clouds using the measured atmospheric transmittance of global radiation (also referred to as clearness index). The atmospheric transmittance is obtained using a multifilter rotating shadowband radiometer (MFRSR) as,

$$T = \frac{\text{GHI}^{415\,\text{nm}}}{\text{GHI}_0^{415\,\text{nm}}}, \tag{7}$$

where $\text{GHI}^{415\,\text{nm}}$ is the global horizontal irradiance, and $\text{GHI}_0^{415\,\text{nm}}$ is the top of the atmosphere GHI, both at a wavelength of 415 nm. The MFRSR measurements at a wavelength of 415 nm is used in Eq. (7), to reduce effects of gaseous absorption. GHI_0 is adjusted from the true TOA GHI to remove τ_a influences on T, by applying Langley regression calibrations from the direct normal irradiance (DNI) on clear skies to the GHI (Harrison et al., 1994; Min et al., 1996b). A discrete ordinate radiative transfer model is applied to identify the τ_c corresponding to the measured T (Min et al., 1996a). By default a cloud effective radius (r_e) of 8 µm is assumed in the Min method, but when liquid water path (LWP) values are available from a microwave radiometer (MWR), then r_e is iteratively solved. r_e is first solved for with Eq. (8) and used as an input in the discrete ordinate model, which provides a different τ_c, which leads to a different r_e and this process is repeated until the changes in τ_c are within a threshold value. Since the Min method uses GHI measurements to estimate τ_c, the τ_c is representative of the sky hemisphere. At ARM Min τ_c is sampled and reported every 20 s.

τ_c is also measured by a MWR. The MWR is a microwave receiver that detects the microwave emissions of the vapor and liquid water molecules. It measures cloud liquid water path (LWP) in the zenith direction within a field of view of 6° (Liljegren et al., 2000; Cadeddu et al., 2013). τ_c can then be estimated as (Stephens et al., 1978)

$$\tau_c \approx \frac{\frac{3}{2}\int LWC\,dz}{\rho_l r_e} = \frac{\frac{3}{2}LWP}{\rho_l r_e}, \tag{8}$$

where LWC is the cloud liquid water content and ρ_l is the density of liquid water. A r_e of 8 µm is assumed, as in the Min method. The MWR has an irregular timestep ranging between 20 to 40 s. The uncertainty in the LWP obtained from the MWR is ±0.03 mm (30 g m^{-2}, Morris et al., 2006) which corresponds to a τ_c of ±5.6 with Eq. (8).

6.2 Validation in overcast conditions with Min algorithm

Data from the Min algorithm is compared to the average τ_c from an entire USI image. Since the Min method assumes overcast skies, only conditions with cloud fraction (CF) > 0.7 are used for this analysis yielding 5197 datapoints (about 43 h of data). The mean transmission of horizontally heterogeneous clouds is higher than the transmission of a uniform cloud with the same mean optical depth (Hinkelman et al., 2007). This is caused by the nonlinear relationship between τ_c and radiance. To adjust the heterogeneous USI τ_c retrieval to be consistent with the Min method, the average τ_c from the USI image is taken as the geometric mean of the image,

$$\tau_c = \exp(\lceil \log(\tau_c) \rceil) \tag{9}$$

Figure 9 compares results from both methods. An R^2 of 0.93 reflects the high correlation between the two methods. The relative RMSE decreases as τ_c increases as demonstrated in Table 2, with thin clouds ($\tau_c < 5$) having an RMSE of 42.7 % and thick clouds ($\tau_c > 20$) having an RMSE of 18.5 % with the overall RMSE being 23.7 %. These differences in RMSE between τ_c highlight the difficulties in detecting thin clouds correctly.

Title Page

Abstract | Introduction

Conclusions | References

Tables | Figures

|◄ | ►|

◄ | ►

Back | Close

Full Screen / Esc

Printer-friendly Version

Interactive Discussion

6.3 Heterogeneous and homogenous cloud conditions with the microwave radiometer

The RRBR method is compared to τ_c estimates from the microwave radiometer (MWR) using the 12 422 pixels in each USI image with $\vartheta_z < 6°$. Figure 10 shows the comparison of the two methods. Overcast conditions again result in good agreement with RMSE of 6.6 or 48 % and R^2 of 0.91. Since overcast datapoints were already validated in Sect. 6.3 we now focus on cloud fractions of less than 0.7.

The RMSE is 2.33 for the heterogeneous cases, which is well within the uncertainty of the MWR measurements of ± 5.6. The lower correlation of 0.66 between the two methods is probably related (i) the uncertainty of the MWR, (ii) the smaller measurement area ($6°$ angle versus entire hemisphere) combined with temporal and spatial offsets and (iii) the fact that τ_c retrievals under heterogeneous cloud conditions introduce random errors due to incomplete overlap of the field-of-view of the USI and MWR, (iv) 3-D cloud effects and (v) uncertainty in the MWR τ_c related to the assumption of $r_e = 8\,\mu$. While the SHDOM model calculations also assume constant r_e, this only affects the single scattering properties of the cloud, more specifically the phase function. This results in the MWR algorithm being more sensitive to r_e as r_e errors are linearly proportional to MWR errors. A MBE of -10.5 % is observed demonstrating a tendency for the RRBR method to under predict τ_c. This can further be analyzed when MBE is split into τ_c categories. Thick clouds ($\tau_c > 20$) have the highest MBE of -34.2 % compared to thin clouds ($\tau_c < 5$) that have an MBE of -5.1. It is believed that this is caused by 3-D cloud effects. For heterogeneous clouds, the cloud sides are no longer obscured such as those in overcast clouds, this leads to increased cloud illumination relative to overcast clouds. For cloud that are thicker than the radiance peak ($\tau_c = 7.25$) this increased radiance along the sun-facing edge of the cloud results in an under prediction of τ_c. The increase in negative MBE with τ_c highlights this heterogeneous under prediction error in RRBR. This argument is further substantiated by the MBE increasing with the inclusion of overcast MWR measurements. Just like in overcast conditions

(Sect. 6.2), RMSE is highest for thin clouds ($\tau_c < 5$) at 95.6 % and fairly constant at higher τ_c with medium clouds ($5 < \tau_c < 20$) and thick clouds having an RMSE of 45.7 and 44.8 % respectively. The heterogeneous cases are associated with a higher relative RMSE of 82.9 % compared to 23.7 % reported in Sect. 6.2 for the homogeneous Min method.

6.4 DNI measurements

Another option for validation is to calculate τ_c directly from Beer's law using the DNI measurement of the MFRSR, which validates τ_c in the circumsolar region (Fig. 11). Rearranging Beer's law and solving for τ_c we obtain,

$$\tau_{\mathrm{MFRSR}} = -\log\left(\frac{\mathrm{DNI}}{\mathrm{DNI}_0}\right) \cdot \frac{\cos(\theta_0)}{A}, \tag{10}$$

where DNI is the measured DNI from the MFRSR, DNI_0 is clear sky DNI computed with the Ineichen model (Ineichen et al., 2002). $A = 0.43$ is a constant factor to account for the strong forward peak in the phase function of liquid and ice water clouds. A is obtained by applying a linear least squares best fit between the τ_c of the RRBR method taken at the nearest time to the MFRSR measurements. The τ_c of the RRBR method are based on the average measurement for pixels in the solar region ($\vartheta_s < 5°$).

Several modifications to the validation dataset are required. The maximum detectable τ_c is limited for the DNI method because for large τ_c ($\tau_c > 5$) DNI is close to zero and τ_c retrievals from the DNI measurement become noisy. Because of this all clouds with $\tau_c > 5$ are set to $\tau_c = 5$ for both MFRSR and RRBR. Furthermore, at small τ_c ($\tau_c < 2$), in the circumsolar region, it becomes very difficult to distinguish thin clouds ($1 > \tau_c > 2$) from clear sky ($\tau_c = 0$) because of the diffraction patterns caused by the custom aperture. The circular aperture causes a circular diffraction pattern (also referred to as Airy disk) that is misidentified as a circular thin cloud. Since the aperture and lens have slight manufacturing tolerances, the diffraction does not result in a perfect disk and is therefore difficult to correct. The Airy disk causes pixels to be assigned

an optical depth of $2.5 < \tau_c < 3.5$ under clear skies. This leads to clear sky conditions yielding an average $1 < \tau_c < 2$ for the pixels in the circumsolar region. The following correction is implemented: For average USI $\tau_c < 2$, τ_c pixel measurements greater than 2 are removed from the averaging, since they are believed to be caused by the Airy pattern. In clear skies this correction only causes clear pixels to remain with typical average $\tau_c < 0.5$. When thin clouds with $\tau_c < 2$ are observed their pixel to pixel variations are minimal so eliminating any pixels with τ_c greater than 2 does not affect the average as very few pixels are greater than 2.

Additional errors include stray light being greater for small τ_c and having a larger impact on the solar region. If τ_c increases from $\tau_c = 0$, diffuse radiance increases but stray light decreases, leading to two competing factors affecting radiance. For $\tau_c < 1$, the increase in diffuse radiance is much larger than the decrease in stray light but for $1 < \tau_c < 2$ diffuse radiance begins to decrease and stray light continues to decrease resulting in similar radiance to clear sky. Even with the correction the MBE for $\tau_c < 2$ is still high at 169.5 % while the overall MBE is 17.9 % suggesting that clear sky still gets misdetected as thin cloud.

7   Discussion and conclusions

This paper presents an analysis of the atmospheric radiative transfer effects on sky imager cloud detection and retrieval of τ_c using synthetic images produced by the SHDOM. Synthetic images demonstrate that θ_0, τ_c, ϑ_s, and ϑ_z all significantly and often non-linearly and non-monotonically affect radiance I_λ and RBR of sky image pixels. For thin clouds, $I_\lambda(\vartheta_s)$ increases rapidly as it approaches the sun, as a result of the strong forward peak in the cloud phase function. On the other hand, for thick clouds $I_\lambda(\vartheta_s)$ is found to be near constant with solar pixel angle for $\tau_c > 30$. ϑ_z has two main effects, horizon brightening for thin clouds, and horizon darkening for thick clouds. Thick clouds fall in the diffusion regime where I_λ decreases with ϑ_z, but is independent of other parameters.

At a ϑ_s of 45° $I_\lambda(\tau_c)$ is demonstrated to increase with increasing τ_c for thin clouds. It reaches a peak at a τ_c between 0–5, depending on ϑ_s and ϑ_z. At τ_c greater than 5, $I_\lambda(\tau_c)$ decreases with increasing τ_c. Similar characteristics are observed for the RBR although it does not decrease as much after reaching its maximum, making it an effective tool for distinguishing between clear sky and thick clouds. However, neither $I_\lambda(\tau_c)$ nor RBR(τ_c) are monotonic, leading to the difficulties in cloud detection and τ_c characterization with one parameter. The RRBR method combines the RBR and I_λ to overcome the non-monotonic nature of each individual parameters.

Summary statistics of the different validations are presented in Table 2. For overcast skies the RRBR yields τ_c that are consistent with the Min method and microwave radiometer measurements. For heterogeneous cloud fields (cloud fraction < 0.7), comparisons with microwave radiometer (MWR) measurements of LWC at zenith demonstrated that the RRBR method provides τ_c estimates with typical r^2 of 0.66 and RMSE of 2.3 which is well within the uncertainty of the MWR instrument (± 5.6). A RMSE of 0.95 between the USI and DNI retrieved τ_c is observed in the range of $0 < \tau_c < 5$. As demonstrated by the relative RMSE in Table 2, the current method provides relatively accurate τ_c estimates over the range of $20 < \tau_c < 80$, while the relative RMSE is larger for $\tau_c < 5$. Since τ_c is exponentially related to surface irradiance, accurate τ_c estimates between 0-10 are the most crucial for solar forecasting and unfortunately are also some of the most difficult to correctly identify.

Characterizing the cloud heterogeneity effects may improve the RRBR method. As the RRBR method is based on interpolants developed from simulations of homogeneous overcast skies, cloud heterogeneity violates the assumptions and is assumed to be the leading source of errors. Errors due to cloud heterogeneity have been analyzed mainly in the context of satellite remote sensing. Varnai et al. (1998) and Chambers et al. (1997) observed that the spatial reflectance variation is smoother than variations in τ_c. They hypothesized that optically thicker clouds would scatter more light to their thinner neighboring clouds causing the thinner clouds to appear brighter and thicker (looking from space), while the thinner clouds would scatter less light to the thicker

F. A. Mejia et al.

clouds making them appear darker and thinner than expected for a homogeneous cloud scene. A similar but opposite effect is observed in ground based imagery, where thicker clouds shade their neighboring thinner clouds making them appear darker and thicker but this effect is moderated by the location of the sun relative to the clouds. Figure 9 also shows that sun-facing cloud edges scatter more light, increasing I_λ, and leading to thinner τ_c estimates than the cloud edges on the opposite side. Cloud edges facing away from the sun will be shaded by the rest of the cloud and will be estimated as being thicker. These 3-dimensional effects introduce noise in RRBR estimations of τ_c.

Although the current method is based on results from homogeneous simulations – outside of the cloud edges – the RRBR method is demonstrated to be reasonably accurate based on qualitative comparisons and validations against other ground measurements. This pixel-by-pixel τ_c allows an estimate of the contribution of each individual pixel to the DNI, GHI and diffuse horizontal irradiance at the surface. Solar forecasting will benefit in two ways: (i) Static fields of τ_c can be used to spatially modulate surface irradiance fields beyond the standard binary (clear - cloudy) solar irradiance, either in 1D similar to Eq. (9) or using the homogeneous results from SHDOM simulations from a look-up table. (ii) Temporal evolution of τ_c can be used to extrapolate future cloud τ_c resulting from cloud dynamics. At present, τ_c is assumed to be steady as the cloud field is advected. An analysis of τ_c evolution especially for individual cumulus or stratocumulus clouds through a timeseries of the τ_c could improve solar forecast accuracy and extend forecast horizon. For example, stratocumulus clouds that tend to form overcast layers in coastal southern California thin during the mornings and then break up rapidly over land. The RRBR can detect the cloud thinning rate and forecast break-up time.

References

Cadeddu, M. P., Liljegren, J. C., and Turner, D. D.: The Atmospheric radiation measurement (ARM) program network of microwave radiometers: instrumentation, data, and retrievals, Atmos. Meas. Tech., 6, 2359–2372, doi:10.5194/amt-6-2359-2013, 2013.

Cahalan, R. F., Oreopoulos, L., Marshak, A., Evans, K. F., Davis, A. B., Pincus, R., Yetzer, K. H., Mayer, B., Davies, R., and Ackerman, T. P.: The I3RC-Bringing together the most advanced radiative transfer tools for cloudy atmospheres, B. Am. Meteorol. Soc., 86, 1275–1293, 2005.

Calbo, J. and Sabburg, J.: Feature extraction from whole-sky ground-based images for cloud-type recognition, J. Atmos. Ocean. Technol., 25, 3–14, 2008.

Cazorla, A., Olmo, F. J., and Alados-Arboledas, L.: Development of a sky imager for cloud cover assessment, J. Opt. Soc. Am. A, 25, 29–39, 2008.

Chambers, L. H., Wielicki, B. A., and Evans, K. F.: Accuracy of the independent pixel approximation for satellite estimates of oceanic boundary layer cloud optical depth, J. Geophys. Res.-Atmos., 102, 1779–1794, 1997.

Chow, C. W., Urquhart, B., Lave, M., Dominguez, A., Kleissl, J., Shields, J., and Washom, B.: Intra-hour forecasting with a total sky imager at the UC San Diego solar energy testbed, Solar Energy, 85, 2881–2893, 2011.

Evans, K. F.: The spherical harmonics discrete ordinate method for three-dimensional atmospheric radiative transfer, J. Atmos. Sci., 55, 429–446, 1998.

Gauchet, C., Blanc, P., Espinar, B., Charbonnier, B., and Demengel, D.: Surface solar irradiance estimation with low-cost fish-eye camera, in: Workshop on Remote Sensing Measurements for Renewable Energy, 2012.

Ghonima, M. S., Urquhart, B., Chow, C. W., Shields, J. E., Cazorla, A., and Kleissl, J.: A method for cloud detection and opacity classification based on ground based sky imagery, Atmos. Meas. Tech., 5, 2881–2892, doi:10.5194/amt-5-2881-2012, 2012.

Hammer, A., Heinemann, D., Lorenz, E., and Lückehe, B.: Short-term forecasting of solar radiation: a statistical approach using satellite data, Solar Energy, 67, 139–150, 1999.

Harrison, L. and Michalsky, J.: Objective algorithms for the retrieval of optical depths from ground-based measurements, Appl. Opt., 33, 5126–5132, 1994.

Heinle, A., Macke, A., and Srivastav, A.: Automatic cloud classification of whole sky images, Atmos. Meas. Tech., 3, 557–567, doi:10.5194/amt-3-557-2010, 2010.

Title Page

Abstract | Introduction

Conclusions | References

Tables | Figures

◀ | ▶|

◀ | ▶

Back | Close

Full Screen / Esc

Printer-friendly Version

Interactive Discussion

Hinkelman, L. M., Evans, K. F., Clothiaux, E. E., Ackerman, T. P. ,and Stackhouse Jr, P. W.: The effect of cumulus cloud field anisotropy on domain-averaged solar fluxes and atmospheric heating rates, J. Atmos. Sci., 64, 3499–3520, 2007.

Holben, B., Eck, T., Slutsker, I., Tanre, D., Buis, J., Setzer, A., Vermote, E., Reagan, J., Kaufman, Y., and Nakajima, T.: AERONET—A federated instrument network and data archive for aerosol characterization, Remote Sens. Environ., 66, 1–16, 1998.

Holben, B., Tanre, D., Smirnov, A., Eck, T., Slutsker, I., Abuhassan, N., Newcomb, W., Schafer, J., Chatenet, B., and Lavenu, F.: An emerging ground-based aerosol climatology: Aerosol optical depth from AERONET, J. Geophys. Res.-Atmos., 106, 12067–12097, 2001.

Ineichen, P. and Perez, R.: A new airmass independent formulation for the Linke turbidity coefficient, Solar Energy, 73, 151–157, 2002.

Kassianov, E., Long, C. N., and Christy, J.: Cloud-base-height estimation from paired ground-based hemispherical observations, J. Appl. Meteorol., 44, 1221–1233, 2005.

Kegelmeyer Jr, W.: Extraction of cloud statistics from whole sky imaging cameras, 1994.

Koehler, T., Johnson, R., and Shields, J.: Status of the whole sky imager database, in: Proc. Cloud Impacts on DOD Operations and Systems – 1991 Conference, 77–80, 1991.

Liljegren, J. C.: Automatic self-calibration of ARM microwave radiometers, VSP Press, 2000.

Long, C. N., Sabburg, J. M., Calbó, J., and Pagès, D.: Retrieving cloud characteristics from ground-based daytime color all-sky images, J. Atmos. Ocean. Technol., 23, 633–652, 2006.

Lorenz, E., Hurka, J., Heinemann, D., and Beyer, H. G.: Irradiance forecasting for the power prediction of grid-connected photovoltaic systems, Selected Topics in Applied Earth Observations and Remote Sensing, IEEE J. Sel. Top. Appl., 2, 2–10, 2009.

Mantelli Neto, S. L., von Wangenheim, A., Pereira, E. B., and Comunello, E.: The use of Euclidean geometric distance on RGB color space for the classification of sky and cloud patterns, J. Atmos. Ocean. Technol., 27, 1504–1517, 2010.

Marshak, A. and Davis, A.: 3-D radiative transfer in cloudy atmospheres, Springer Science & Business Media, 2005.

Martínez-Chico, M., Batlles, F. ,and Bosch, J.: Cloud classification in a mediterranean location using radiation data and sky images, Energy, 36, 4055–4062, 2011.

Mathiesen, P. and Kleissl, J.: Evaluation of numerical weather prediction for intra-day solar forecasting in the continental United States, Solar Energy, 85, 967–977, 2011.

Mathiesen, P., Collier, C., and Kleissl, J.: Case Studies with the Weather and Research Fore-casting Model at GL-Garrad Hassan, in: Solar Resource Assessment and Forecasting, 1, edited by: Kleissl, J., Elsevier, 358–381, 2013.

McGuffe, K. and Henderson-Sellers, A.: Almost a century of "imaging" clouds over the whole-sky dome, B. Am. Meteorol. Soc., 70, 1243–1253, 1989.

Min, Q. and Harrison, L. C.: An adjoint formulation of the radiative transfer method, J. Geophys. Res.-Atmos., 101, 1635–1640, 1996a.

Min, Q. and Harrison, L. C.: Cloud properties derived from surface MFRSR measurements and comparison with GOES results at the ARM SGP Site, Geophys. Res. Lett., 23, 1641–1644, 1996b.

Min, Q., Duan, M., and Marchand, R.: Validation of surface retrieved cloud optical proper-ties with in situ measurements at the Atmospheric Radiation Measurement Program (ARM) South Great Plains site, J. Geophys. Res.-Atmos., 108, 4547, doi:10.1029/2003JD003385, 2003.

Miyamoto, K.: Fish eye lens, JOSA, 54, 1060–1061, 1964.

Morris, V.: Microwave radiometer (MWR) handbook, ARM-TR016, 1–20, 2006.

Nakajima, T. and King, M. D.: Determination of the optical thickness and effective particle radius of clouds from reflected solar radiation measurements, Part I: Theory, J. Atmos. Sci., 47, 1878–1893, 1990.

Pfister, G., McKenzie, R. L., Liley, J. B., Thomas, A., Forgan, B. W., and Long, C. N.: Cloud cov-erage based on all-sky imaging and its impact on surface solar irradiance, J. Appl. Meteorol., 42, 1421–1434, 2003.

Pincus, R. and Evans, K. F.: Computational cost and accuracy in calculating three-dimensional radiative transfer: Results for new implementations of Monte Carlo and SHDOM, J. Atmos. Sci., 66, 3131–3146, 2009.

Román, R., Antón, M., Cazorla, A., de Miguel, A., Olmo, F. J., Bilbao, J., and Alados-Arboledas, L.: Calibration of an all-sky camera for obtaining sky radiance at three wavelengths, Atmos. Meas. Tech., 5, 2013–2024, doi:10.5194/amt-5-2013-2012, 2012.

Roy, G., Hayman, S., and Julian, W.: Sky analysis from CCD images: cloud cover, Lighting Res. Technol., 33, 211–221, 2001.

Seiz, G., Shields, J., Feister, U., Baltsavias, E., and Gruen, A.: Cloud mapping with ground-based photogrammetric cameras, Int. J. Remote Sens., 28, 2001–2032, 2007.

Title Page

Abstract | Introduction

Conclusions | References

Tables | Figures

|◄ | ►|

◄ | ►

Back | Close

Full Screen / Esc

Printer-friendly Version

Interactive Discussion

Shields, J., Johnson, R., and Koehler, T.: Automated whole sky imaging systems for cloud field assessment, in: Fourth Symposium on Global Change Studies, Am. Meteorol. Soc., 228–231, 1993.

Souza-Echer, M., Pereira, E., Bins, L. ,and Andrade, M.: A simple method for the assessment of the cloud cover state in high-latitude regions by a ground-based digital camera, J. Atmos. Ocean. Technol., 23, 437–447, 2006.

Stephens, G.: Radiation profiles in extended water clouds, II: Parameterization schemes, J. Atmos. Sci., 35, 2123–2132, 1978.

Urquhart, B., Ghonima, M., Dung, A., Kurtz, B., Chow, C. W., and Kleissl, J.: Sky Imaging Systems for Short-term Forecasting, in: Solar Resource Assessment and Forecasting, 1, edited by: Kleissl, J., Elsevier, 196–229, 2013.

Urquhart, B., Kurtz, B., Dahlin, E., Ghonima, M., Shields, J. E., and Kleissl, J.: Development of a sky imaging system for short-term solar power forecasting, Atmos. Meas. Tech., 8, 875–890, doi:10.5194/amt-8-875-2015, 2015.

Varnai, T.: Influence of Three-Dimensional Radiative Effects on the Spatial Distribution of Short-wave Cloud Reflection, J. Atmos. Sci., 57, 216–227, 1998.

Title Page

Abstract | Introduction

Conclusions | References

Tables | Figures

|◄ | ►|

◄ | ►

Back | Close

Full Screen / Esc

Printer-friendly Version

Interactive Discussion

Table 1. Atmospheric radiative properties for the ARM site used as input to SHDOM. τ_a and Rayleigh optical depth are averages for the year 2013 from AERONET data.

	Red (620 nm)	Green (520 nm)	Blue (450 nm)
τ_a [–]	0.0784	0.1010	0.1212
Rayleigh optical depth [–]	0.0875	0.1627	0.2296
Effective Radius (R_e) [µm]	3.9	3.9	3.9
Aerosol R_e distribution	Lognormal	Lognormal	Lognormal
Refractive index [–]	1.42–0.002i	1.41–0.002i	1.40–0.002i

Table 2. Statistics of RRBR validation against the Min method in overcast skies, microwave radiometer measurements, and DNI measurements from the MFRSR.

Method	CF	τ_c	R^2	RMSE [–]	RMSE [%]	MAE [%]	MBE [%]
Min	>0.7	All	0.93	5.6	23.7	17.6	−5.4
Min	>0.7	<5	0.16	1.5	42.7	33.9	22.8
Min	>0.7	>5 & <20	0.70	3.3	29.7	24.1	−15.5
Min	>0.7	>20	0.85	7.8	18.5	15.5	−3.6
MWR	All	All	0.91	6.6	47.8	28.6	15.4
MWR	<0.7	All	0.66	2.3	82.9	49.6	−10.5
MWR	<0.7	<5	0.36	1.5	95.6	65.9	−5.1
MWR	<0.7	>5 & <20	0.23	3.8	45.7	35.1	−11.9
MWR	<0.7	>20	0.50	13.6	44.8	37.5	−34.2
DNI	All	All	0.81	0.95	44.0	33.1	17.9
DNI	All	<2	0.28	0.98	213.3	179.9	169.5
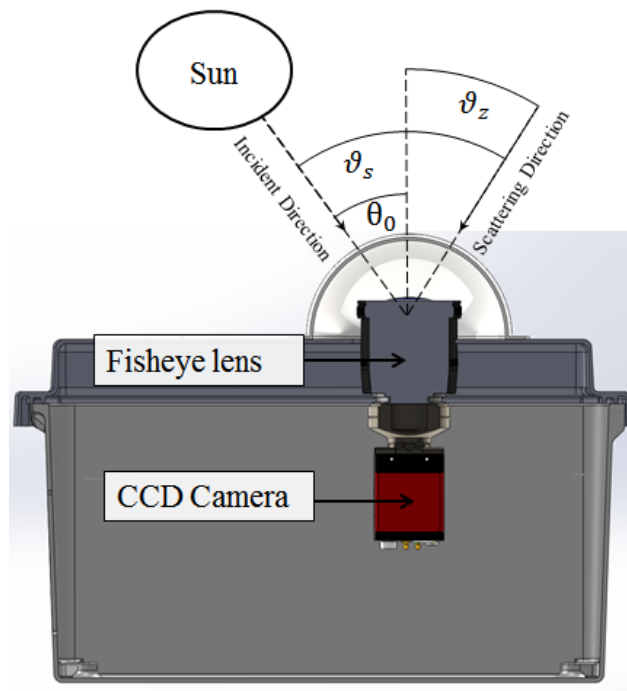
Figure 1. Diagram of the UCSD sky imager (USI) and related solar and sky geometries. θ_0 is the solar zenith angle. The ϑ_s is the angle subtended by the vector pointing at the sun and the vector pointing at the pixel in question. The ϑ_z is the angle formed by the vector pointing at the pixel in question and zenith. It is important to note that $\vartheta_s = \theta_0 + \vartheta_z$ only holds in 2-D, but not in 3-D as demonstrated in Fig. 2.
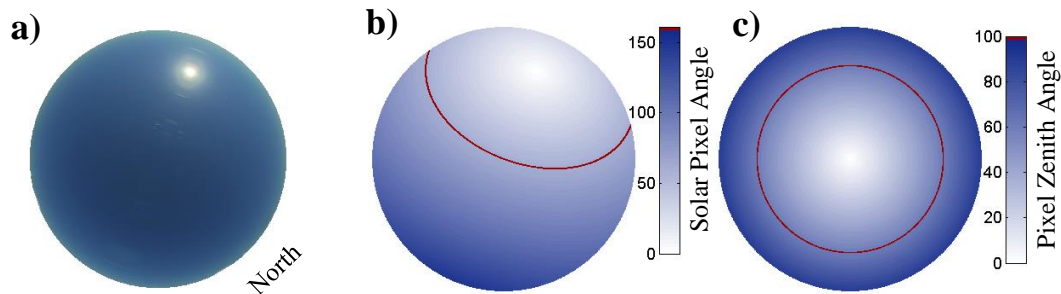
Figure 2. (a) Clear USI image from a clear sky library (CSL) for a solar zenith angle of 60° on 26 March 2013, 15:00 UTC, **(b)** Solar Pixel Angles, and **(c)** Pixel Zenith Angles. The red line in Fig. 2b. highlights the pixels with $\vartheta_s = 60°$, while the red line in Fig. 2c highlights the pixels with $\vartheta_z = 60°$, which are often used in the following chapters to illustrate relationships with cloud optical depth and radiance. North is located on the bottom right corner of the image.
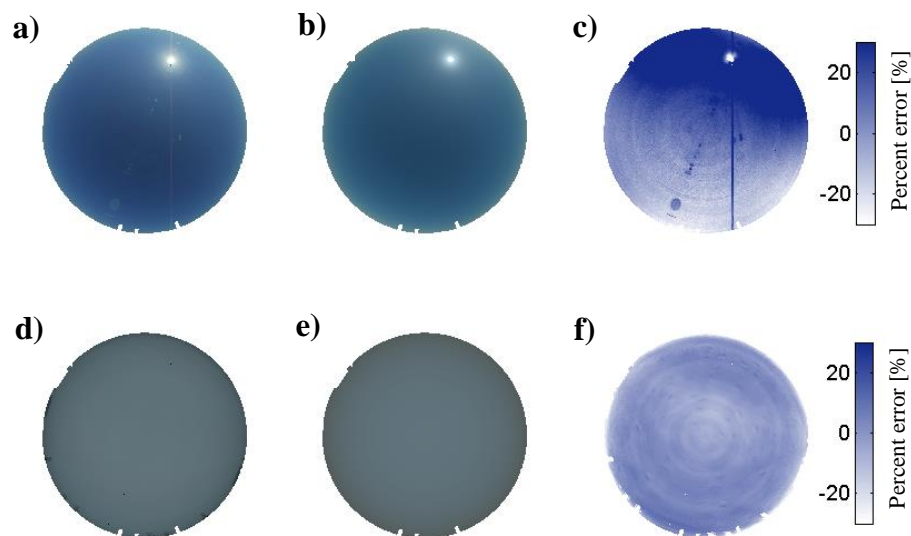
Figure 3. (a) Clear sky USI image for 26 March 2013, 15:00 UTC, **(b)** synthetic image from SHDOM for τ_c of 0 and θ_0 of 60°, **(c)** percent error in red channel radiance, **(d)** USI image for 05 May 2013, 14:08 UTC **(e)** Synthetic Image for θ_0 of 60° and τ_c of 30, and **(f)** percent error in red channel radiance.
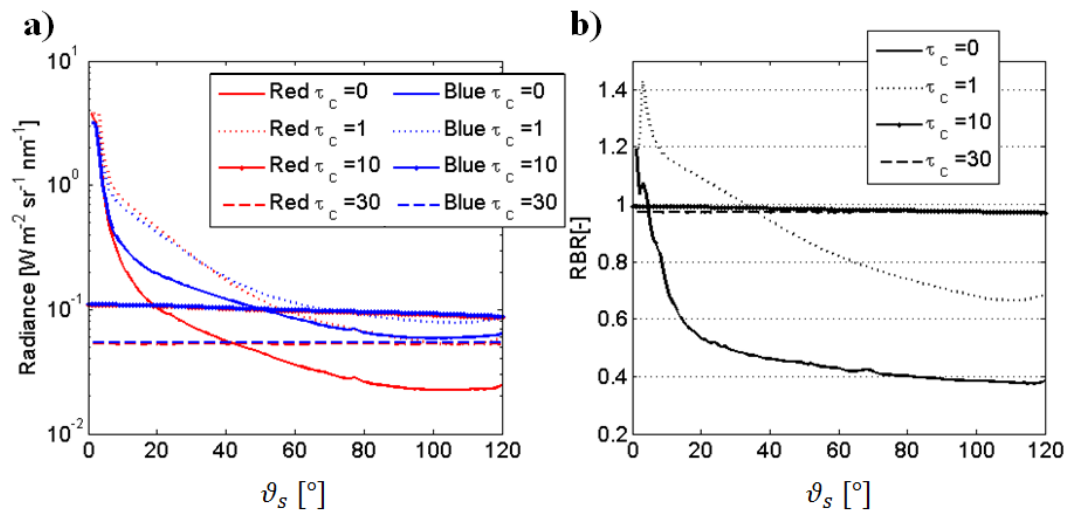
Figure 4. (a) SHDOM red channel radiance over various sun pixel angles (ϑ_s) at $\vartheta_z = 60°$, and $\theta_0 = 60°$ (Pixels used for Fig. 4 are highlighted as a red line in Fig. 2c). Results are shown for different cloud optical depths from clear ($\tau_c = 0$) to thick clouds. **(b)** RBR as a function of ϑ_s at constant $\vartheta_z = 60°$ and $\theta_0 = 60°$.
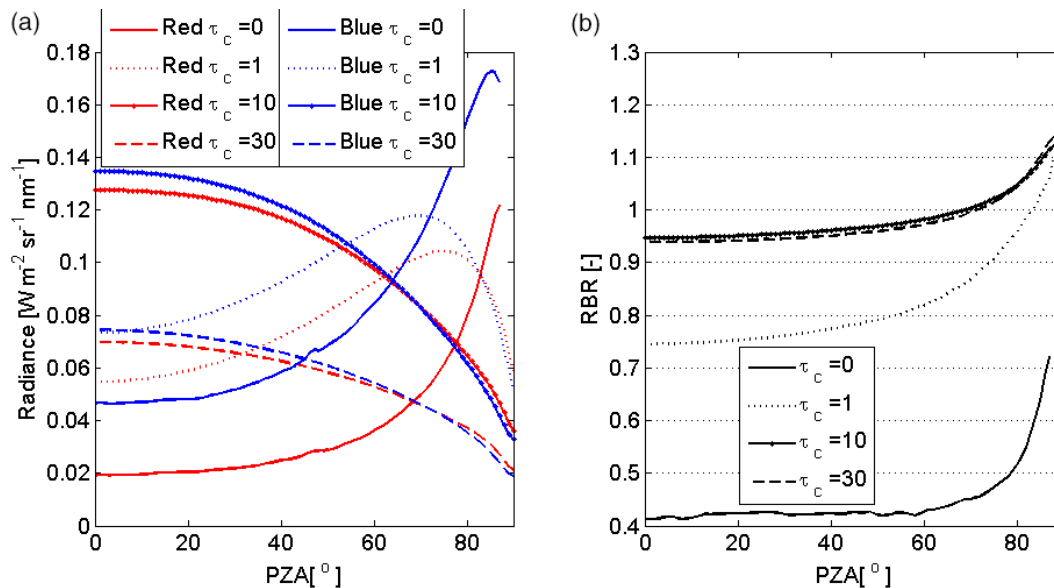
Figure 5. (a) Red and blue channel radiances and **(b)** RBR over various ϑ_z at constant $\vartheta_s = 60°$, and $\theta_0 = 60°$. Pixels used for Fig. 5 are highlighted as a red line in Fig. 2b.
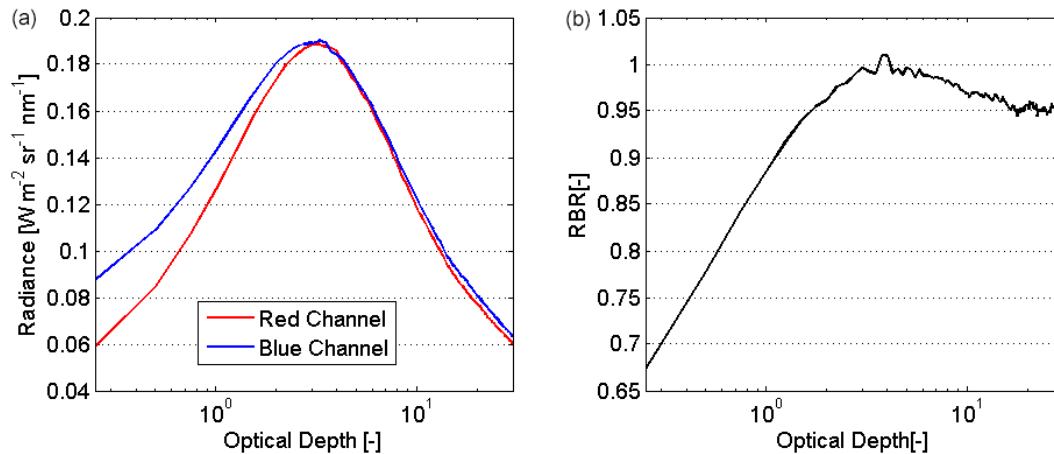
Figure 6. Red and blue channel radiance **(a)** and RBR **(b)** vs. τ_c for ϑ_s of 45°, θ_0 of 60° and ϑ_z of 45°.
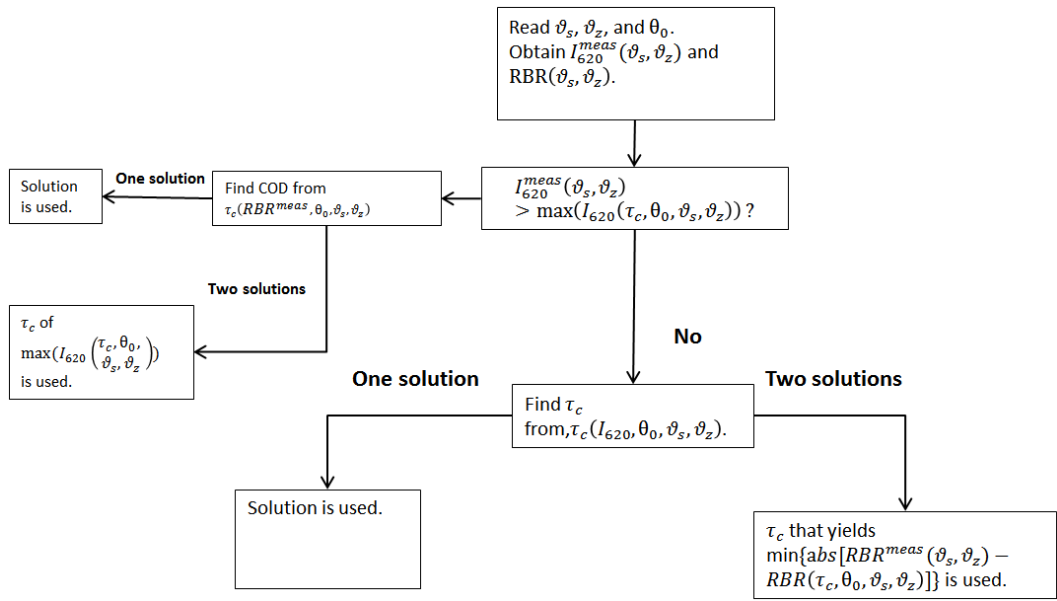
Figure 7. Flowchart of the radiance red blue ratio (RRBR) method for τ_c estimation. If $I_{620}^{\text{meas}}(\vartheta_s, \vartheta_z)$ is saturated (e.g. in the solar disk), τ_c is assigned Not-a-Number.

Figure 8. Comparison of RRBR τ_c retrievals from the sky imager versus the Min method applied to MFRSR measurements for USI cloud fractions greater than 0.7. USI results are averaged over the hemisphere as shown in Eq. (9).
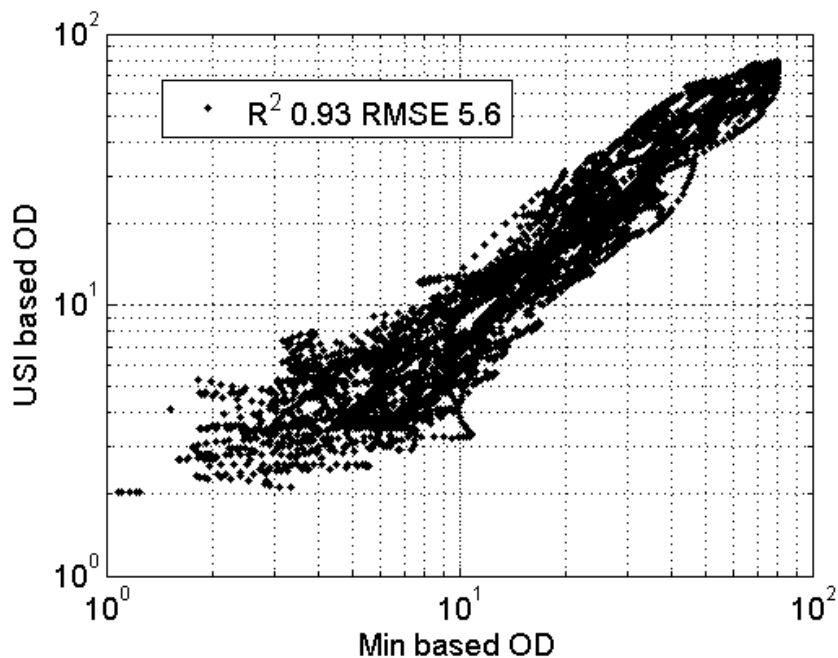
Figure 9. Comparison of USI RRBR versus MWR measurements of cloud optical depth for CF < 0.7 in black and CF > 0.7 in red.
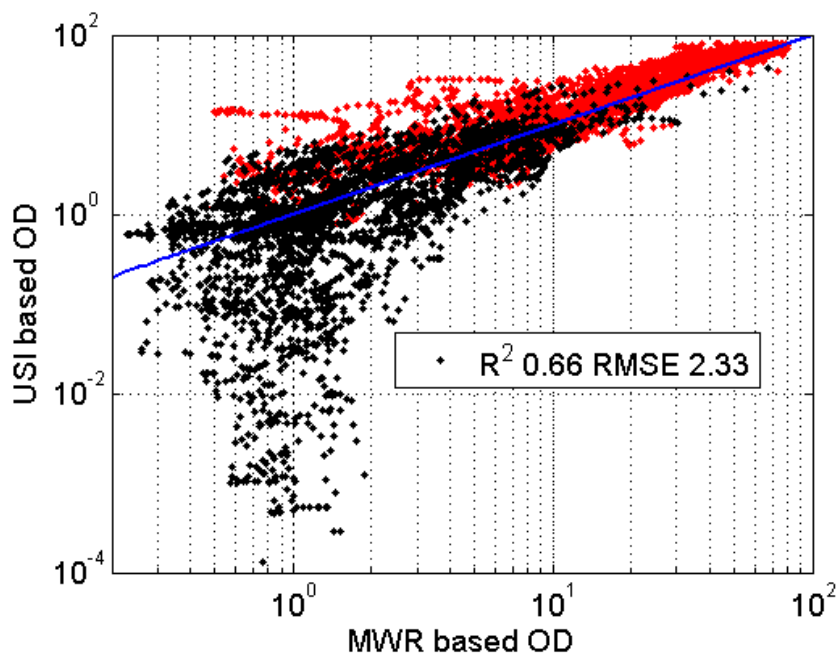
Figure 10. Comparison of RRBR versus DNI method of cloud optical depth retrieval. Since τ_c becomes unreliable for small DNI $\tau_c > 5$ are identified as $\tau_c = 5$ to illustrate that thick clouds are mostly identified correctly.